

**MAX-PLANCK-INSTITUT FÜR PLASMAPHYSIK**  
**GARCHING BEI MÜNCHEN**

Improvement of the SUPERCOIL System Code

Part II

(fatigue in the TF coils)

M. Söll

IPP 4/226

Dezember 1985

*Die nachstehende Arbeit wurde im Rahmen des Vertrages zwischen dem  
Max-Planck-Institut für Plasmaphysik und der Europäischen Atomgemeinschaft über die  
Zusammenarbeit auf dem Gebiete der Plasmaphysik durchgeführt.*

# Improvement of the SUPERCOIL System Code

## Part II

(fatigue in the TF coils)

M. Söll

IPP 4/226

Dezember 1985

### Abstract

This report describes the part of the NET/84-042/PH contract relating to fatigue problems with TF coils due to the influence of the poloidal magnetic field.

A model is developed on the basis of the crack growth rate concept which allows the lifetime of TF coils to be predicted. The stresses induced in the TF coils by the PF magnetic fields are calculated with an analytical model. The first step in the model is to calculate the magnetic force per unit length produced in the TF coil by the poloidal magnetic field. The second step is to calculate the induced stresses by considering realistic lateral support structures. With these additional stresses (additional with respect to the static stresses produced by the TF field), the maximum tolerable number of cycles is determined by the Paris law. Within the analytical model use is made of a further design criterion following from torsional moment yielding shear stresses. The accuracy of the analytical model is tested with finite-element calculations.

## I. Basic relations and considerations

This section discusses the basic definitions and relations of fracture mechanics which are used for calculating the lifetime of the TF coils in SUPERCOIL /1/. The TF coils are mechanically loaded by the toroidal magnetic field forces and by the forces produced by the poloidal magnetic fields (forces due to thermal processes are not taken into account). The magnetic forces produce stresses in the TF coils which are defined as  $\sigma_{TFT}$  (produced by the toroidal field  $B_T$ ) and  $\sigma_{TFP}$  (produced by the toroidal field  $B_P$ ). With optimized ideal constant-tension TF coils having a D-shape /2,3/ the  $\sigma_{TFT}$  stresses are pure tension stresses. The poloidal field produces forces in the TF coils which act as bending and torsional moments. The bending moment produces additional tension stresses and the torsional moment shear stresses. A schematic time pattern for the tension stress is shown in Fig. 1; it is assumed that the poloidal field coils are loaded from 0 to  $B_{pmax}$  and back.

The stress ratio  $R$ , defined as

$$R = \sigma_{min} / \sigma_{max}, \quad (1)$$

is  $\sigma_{TFT} / (\sigma_{TFT} + \sigma_{TFP}) < 1$  for the TF coils and  $R = 0$  for the PF coils.

The stress distribution in the vicinity of the crack (see Fig. 1b) is given by

$$\begin{bmatrix} \sigma_{xx}^a \\ \sigma_{yy}^a \\ \sigma_{xy}^a \end{bmatrix} = \frac{K}{\sqrt{2\pi r}} \cos \theta/2 \begin{bmatrix} 1 - \sin \theta/2 \cdot \sin 3\theta/2 \\ 1 + \sin \theta/2 \cdot \sin 3\theta/2 \\ \sin \theta/2 \cos 3\theta/2 \end{bmatrix} \quad (2)$$

for the case that normal "external stresses"  $\sigma_{xx}$ ,  $\sigma_{yy}$  are applied. The relations (2) are simplified expressions /4/ derived from the complex stress analysis of Westergaard /28/.

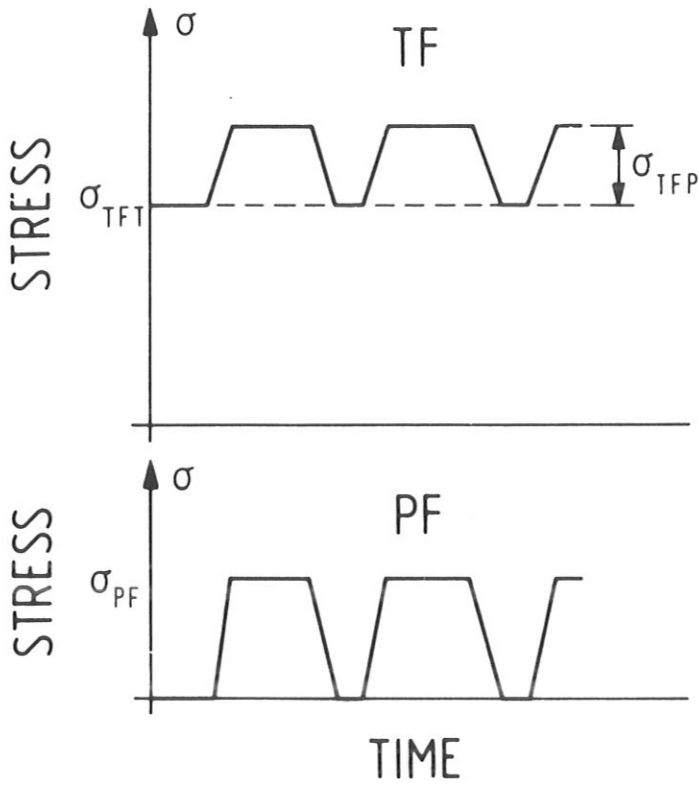


Fig. 1a: Applied (external) stresses in the TF coil ( $\sigma_{TF}$ ) and PF coil ( $\sigma_{PF}$ ) due to current increase in the PF coil

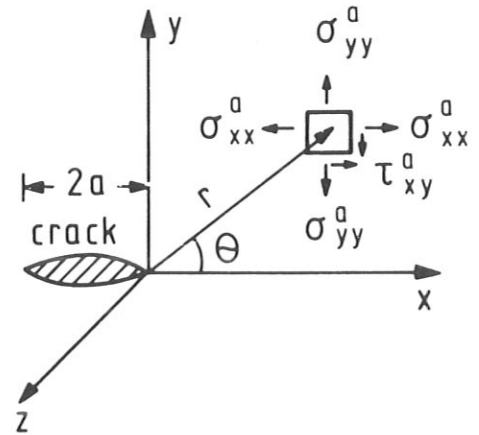


Fig. 1b: Stress components in the vicinity of a crack

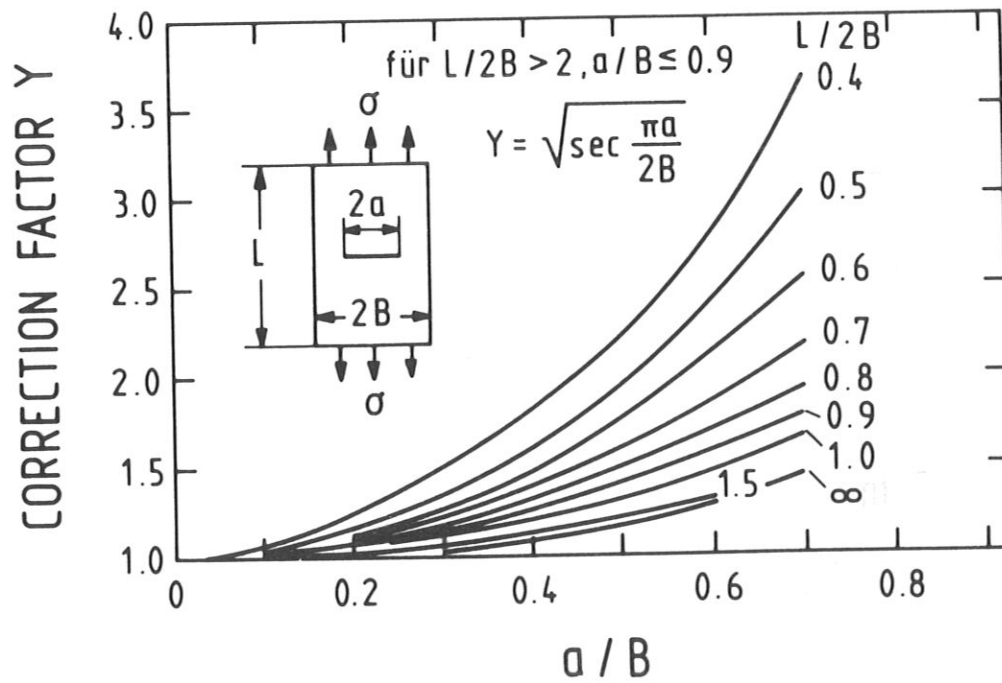


Fig. 2: Correction factor  $Y$  for a material with deeply buried flaws [4].

K is the so-called stress intensity factor. For an infinitely extended specimen K is given by

$$K = \sigma \sqrt{\pi a} , \quad (3)$$

and for a finite specimen by

$$K = \sigma \sqrt{\pi a} Y , \quad (4)$$

where Y is the geometrical correction factor (see Fig. 2); for  $L/2B > 2$  and  $a/B \leq 0.9$  Y can be calculated from [4/

$$Y = \left[ \frac{1}{\cos\left(\frac{\pi a}{2B}\right)} \right]^{1/2} \quad (5)$$

Using the expression for the crack energy [4/ it can be shown that the stress intensity factor K is determined by the material properties, the elastic modules and the compliance and specimen geometry [4/.

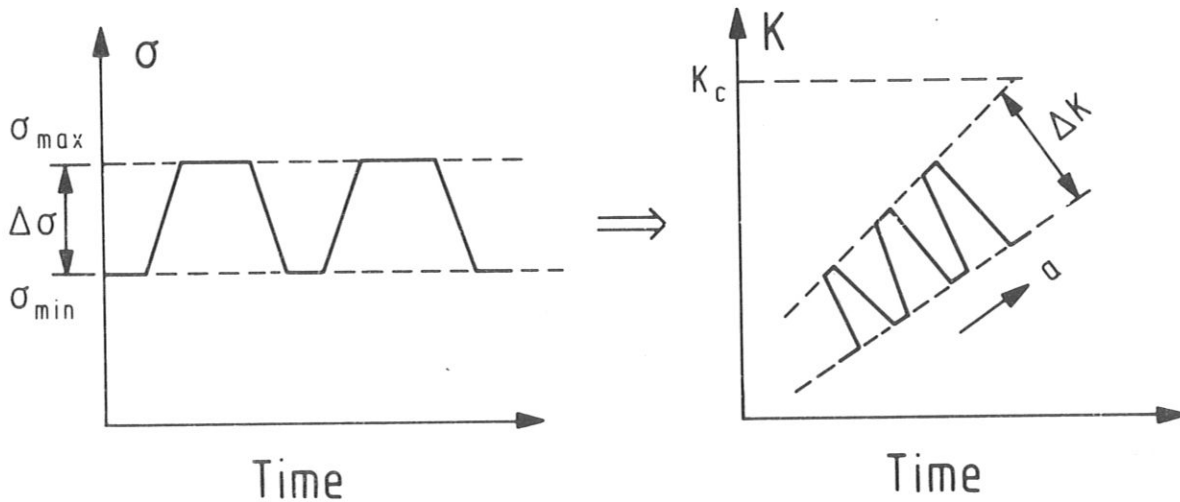


Fig. 3: Dependence of the stress and stress intensity factor K on time and crack length a.

With eqs. (4) and (5) the stress  $\sigma$  and the stress intensity factor  $K$  during a crack growth process are related as schematically shown in Fig. 3.

The value of  $\Delta K$  increases accordingly with increasing crack size as

$$\Delta K = \Delta \sigma \sqrt{\pi a} Y . \quad (6)$$

Fracture occurs if a critical  $\sigma$  value ( $\sigma_c$ ) is exceeded. Instead of using  $\sigma_c$  as critical value it is more conveniently to use the critical stress intensity  $K_c$ , which (like  $\sigma_c$ ) depends on the material properties and specimen geometry (see rels. (3) and (4)) /4/. Experiments show that varying the specimen thickness yields a minimum  $K_c$  value. This minimum  $K_c$  value corresponds to thick samples where the applied stress is perpendicular to the crack surface. These experimental results show that a plane strain situation is present when fracture occurs. The minimum  $K_c$  value is therefore defined as  $K_{ic}$ , the plane strain fracture toughness  $K_{ic}$ . To calculate the critical crack size  $a_c$ , which defines the maximum crack size above which fracture occurs, the  $K_{ic}$  value is used. There are two reasons for using  $K_{ic}$  instead of  $K_c$ . First, the samples (coil housing or conductors) are generally thick in comparison with  $a/B$  values and, second, using the minimum  $K_c$  value provides additional safety for cases where the plane strain condition is not strictly present.

The critical crack size follows from

$$a_c = \left[ \frac{K_{ic}}{S \cdot Y \cdot \sigma_{\max} \sqrt{\pi}} \right]^2 , \quad (7)$$

where  $S$  is a safety factor, a value of two generally being used /8/.

The governing quantity in fracture mechanics is the crack growth rate  $da/dN$  which is a function of  $\Delta K$ , as experiments show. Plotting  $\log da/dN$  versus  $\log \Delta K$  yields the typical curve in Fig. 4.

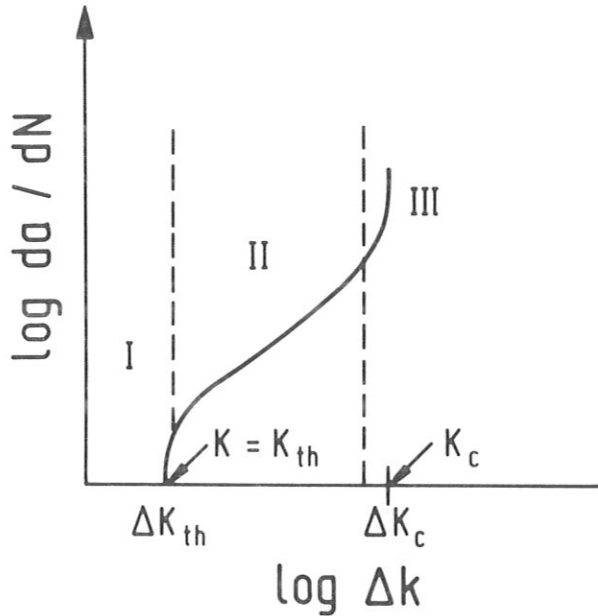


Fig. 4:

Schematic presentation of the crack growth rate versus  $\Delta K$  in log-log coordinates

Three distinct regions can be distinguished. The first is characterized by low  $\Delta K$  values and low  $da/dN$  values. If  $\Delta K$  is smaller than the threshold level  $\Delta K_{th}$ , fatigue failure is quite unlikely. The  $\Delta K_{th}$  values for engineering materials are, however, in the range of a few per cent of the  $\Delta K_c$  value and therefore operation of the structure below  $\Delta K_{th}$  is uneconomical in most cases and leads to heavy structures. Possible mechanisms for the fact that no crack growth occurs for  $\Delta K < \Delta K_{th}$  are given in Ref. 4. For steels  $\Delta K_{th}$  is related to the Young's modulus  $E$  ( $E$  in MPa) as follows /4/:

$$\Delta K_{th}(R=0) = 2.75 \times 10^{-5} \times E \quad (8)$$

$$\Delta K_{th}(R) = \Delta K_{th}(R=0) \times (1-R)^{0.31} \quad (9)$$

The second region is characterized by a linear relation between  $\log da/dN$  and  $\log \Delta K$ . The transition between region I and II lies typically in the range of  $\Delta K = 10 \text{ MPa } \sqrt{\text{m}}$ . Most investigations on the crack growth rate were carried out in region II (see Ref. 5, where an extensive collection of fatigue data is given). Region II can be described by the Paris equation

$$\frac{da}{dN} = C \cdot \Delta K^n, \quad (10)$$

where  $C$  and  $n$  are material data. With eq. (6) and the assumption that  $Y$  does not depend on the crack length  $a$  (see Fig. 2) the Paris equation can be analytically integrated to determine how the number  $N_F$  of cycles applied to the specimen is related to the initial crack length  $a_0$  and a final crack length  $a_F$ :

$$N_F = \frac{2}{(n-2)C \cdot Y^n \Delta \sigma^n \cdot \pi^{n/2}} \left\{ \frac{1}{a_0^{(n-2)/2}} - \frac{1}{a_F^{(n-2)/2}} \right\} \quad n \neq 2, \quad (11)$$

$$N_F = \frac{1}{C \pi \Delta \sigma^2 Y^2} \ln (a_F/a_0) \quad n=2 \quad (11')$$

[ $C$  in  $m/c \cdot (MPa \sqrt{m})^{-n}$ ,  $\Delta \sigma$  in MPa,  $a$  in m].

The assumption that  $Y$  does not depend on the crack size  $a$  is a rather good one if  $L/2B$  (length to width of the conductor or coil housing) is greater than 1. For the cases discussed in this study  $L/2B \gg 1$ .

As an example, the data for stainless steel AISI 304 and AISI 316 at 4 K are given /9/:  $n = 3.78$ ,  $C = 2.04 \times 10^{-13}$  and  $n = 2.93$ ,  $C = 5.36 \times 10^{-12}$ , respectively. These materials are used for cryogenic applications.

There are investigations in which eq. (10) was extended to take into account the stress ratio  $R$ . One model, the one mostly used, was developed by T. Forman et al. /17/; the Forman theory should be applied if a larger portion of the lifetime  $N_F$  is expected to come from region III or if  $R$  changes during the lifetime:

$$\frac{da}{dN} = \frac{C \Delta K^n}{(1-R)K_c - \Delta K} \quad (12)$$



The integration yields

$$N_F = \frac{2}{C(\Delta\sigma\sqrt{\pi})^n} \left[ \frac{(1-R)K_c}{2-n} \left[ a_F^{(2-n)/2} - a_o^{(2-n)/2} \right] - \frac{\Delta\sigma\sqrt{\pi}}{3-n} \left[ a_F^{(3-n)/2} - a_o^{(3-n)/2} \right] \right] \quad (13)$$

In region III the crack growth rate increases with respect to region II. The transition between regions II and III lies - as extensive exploitation of experimental results show - in the crack growth rate region of  $10^{-4}$  -  $10^{-3}$  mm/cycle /4/. The dependence of  $da/dN$  on  $\Delta K$  is not so well investigated in region III as in region II.

A  $K_{IC}$  value for nitrogen-reinforced AISI 316 at 4 K should be mentioned with respect to the application of this material to superconducting magnets; a high value of 210 MPa  $\sqrt{m}$  was found /8/.

Large superconducting magnets have welds; the question therefore rises as to the fatigue response of the welds. For the 304L and 316L materials and their welds, crack growth rates at 4K were measured in region II /10, 11, 4/.

The fatigue crack growth rate for the welded 304L material used in the Japanese Large Coil casing /11/ shows lower values than the parent material; this can be attributed to the different grain size properties of the weld/bulk metal /5/.

Extensive investigations between the parent 316LN steel and its welds were carried out at Karlsruhe /8, 12, 13/. The fatigue crack growth rate in

region II differs very little between the parent material and their welds. A large difference exists with respect to the  $K_{IC}$  value. For the parent material  $K_{IC}$  is 210 MPa  $\sqrt{m}$ , whereas for its welds  $K_{IC}$  varies between 100 and 165 MPa  $\sqrt{m}$ , depending on the weld type.

## II. Model for the fatigue lifetime calculations

The computer program calculates the stresses  $\sigma_{TFT}$  and  $\sigma_{TFP}$  (see Sec. IV). The maximum applied stress in the TF coil is given by  $\sigma_{max} = \sigma_{TFT} + \sigma_{TFP}$ .

The stresses in the reinforcing material (stainless steel) are calculated according to the ratio of the average E module of the coil winding to the E module of the reinforcing material:

$$\hat{\sigma}_R = \frac{E_R (1+\alpha+\beta)}{E_{SC} + \alpha E_{ST} + \beta E_R}, \quad (14)$$

where  $\alpha$  and  $\beta$  are the normalized cross-sectional areas of the stabilizer and reinforced material;  $\alpha = F_{ST}/F_{SC}$ ,  $\beta = F_R/F_{SC}$ . The values are calculated in the COIL subroutine of SUPERCOIL.

The cycle number  $N$  is calculated self-consistently from the total burn time and burn duration; so when the computer program enters the program part where the fatigue lifetime is determined,  $N$ ,  $\sigma_{max}$  and  $\Delta\sigma$  are given.

The first step consists in calculating the threshold crack size  $a_{th}$  by using /5/

$$a_{th} = \left( \frac{\Delta K_{th}(R) \sqrt{\pi}}{2 \Delta\sigma} \right)^2 \quad (15)$$

( $\Delta K_{th}(R)$ ) follows from rels. (8) and (9). If  $a_o$ , the initial crack size, is larger than  $a_{th}$ , the fatigue crack size may limit the lifetime of the specimen. If  $a_o$  is smaller than  $a_{th}$ , the program stops.

For the case  $a_o > a_{th}$  the second step is to calculate the critical crack length  $a_c$ , which for the TF coils is denoted as  $a_{cT}$  (and for the poloidal field coils as  $a_{cP}$ ). The  $a_c$  values are calculated with eq. (7). The third step is to calculate the final crack size  $a_F$  by using eqs. (11) or (11').

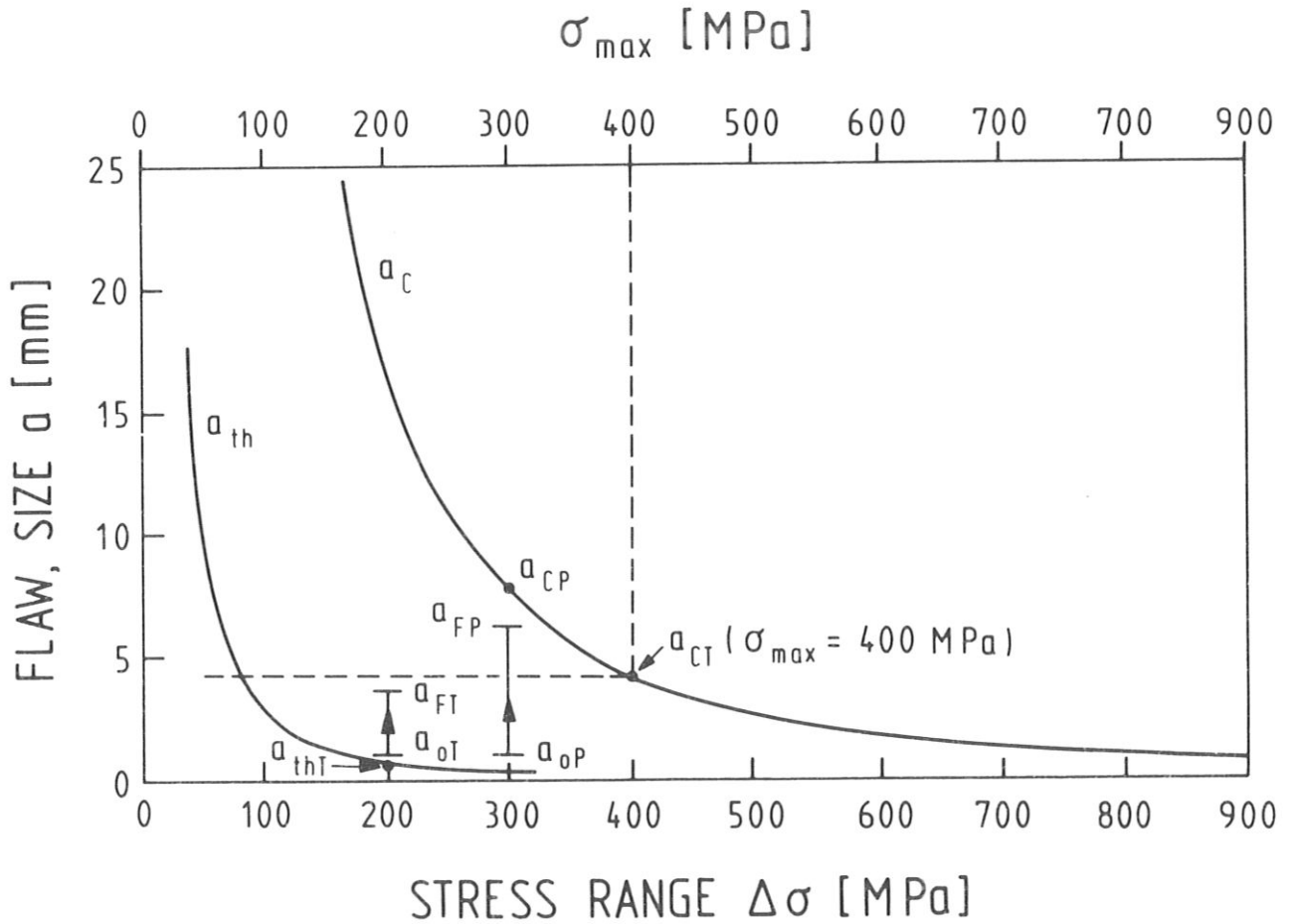


Fig. 5: Dependence of the critical crack size  $a_c$  and the threshold crack size  $a_{th}$  on the stress.

If the final crack size  $a_F$  is smaller than the critical value  $a_c$ , the cycle number can be tolerated as far as the fatigue lifetime of the reinforcing material is concerned. (The model calculations are applied to stainless steel welds.) If  $a_F$  is larger than  $a_c$ , the stress values have to be decreased by an increase of the coil winding thickness or a change in the lateral support structure.

The procedure described above is illustrated by Fig. 5.

The parameters for the curve in Fig. 5 are  $S = 1.8 / 8 /$ ,  $Y = 1.2$ ,  $K_{IC} = 100$  MPa  $\sqrt{m}$ , which is the smallest  $K_{IC}$  value for welded 316 LN material. According to eq. (7), the critical flow size for  $\sigma_{max} = 400$  MPa is  $a_{CT} = 4.26$  mm. From the definition of  $a_{CT}$  it is evident that for a crack length larger than  $2a = 8.52$  mm the specimen is destroyed even by static (single) loading.

The "external" input parameters for the fatigue lifetime calculations based on the procedure described are summarized in Table 1.

$a_o$ [m]	initial flow size
$K_{IC}$ [MP $a\sqrt{m}$ ]	plane strain fracture toughness
$K_{th}$ [MP $a\sqrt{m}$ ]	threshold stress intensity range for $R=0$
$n$	exponent in the Paris equation (10)
$C$ [m/c $\cdot$ (MPa $\sqrt{m}$ ) $^{-n}$ ]	coefficient in the Paris equation (10)
$S$	safety factor
$Y$	geometrical correction value.

Table 1: "External" input parameters for the fatigue lifetime calculations.

The notation "external" means that the parameters are not calculated or used in other parts of the SUPERCOIL computer program.

An "external" parameter which strongly influences the fatigue lifetime is the initial flaw size  $a_0$ . Flaw sizes of  $2a_0 = 2 \text{ mm}$  seem to be a realistic value for welds /8, 13/. The question what value of  $a_0$  would be taken into account is ultimately a question of quality control.

The parameters which have to be taken over from other parts of SUPERCOIL are summarized in Table 2 and are denoted as "internal" input data.

$E_{SC} \text{ [N/m}^2\text{]}$	Young's modulus of the superconductor
$E_{ST} \text{ [N/m}^2\text{]}$	" stabilizer
$E_R \text{ [N/m}^2\text{]}$	" reinforcing material
$\alpha$	ratio $F_{ST}/F_{SC}$
$\beta$	ratio $F_R/F_{SC}$
$\sigma_{TFT} \text{ N/m}^2$	maximal mechanical stress in the TF coil produced by the poloidal magnetic field
$N$	cycle number

Table 2: "Internal" input data used for the fatigue lifetime calculations

As demonstrated by the low-temperature investigations on 316 LN and its welds /8, 12, 13/, the  $K_{IC}$  values of the welds are considerably smaller than the  $K_{IC}$  values for the parent metal, while the fatigue crack growth rates of the two are similar. The material data for welds are therefore used in the fatigue lifetime calculations.

The equations below are written in the sequence used for the calculations, the values with hat being stresses for the reinforcing material; these stresses are used for the fatigue lifetime calculations.

$$\hat{\sigma}_{TFT} = \sigma_{TFT} \cdot \frac{E_R (1+\alpha+\beta)}{E_{SC} + \alpha E_{ST} + \beta E_R}, \quad (16)$$

$$\hat{\sigma}_{TFP} = \sigma_{TFP} \cdot \frac{E_R (1+\alpha+\beta)}{E_{SC} + \alpha E_{ST} + \beta E_R}, \quad (16')$$

$$\hat{\sigma}_{max} = \hat{\sigma}_{TFT} + \hat{\sigma}_{TFP}, \quad (17)$$

$$R = \frac{\hat{\sigma}_{TFT}}{\hat{\sigma}_{TFT} + \hat{\sigma}_{TFP}} \quad (18)$$

$$\Delta K_{th}(R) = 2.75 \cdot 10^{-5} \cdot E \cdot (1-R)^\alpha, \quad (19)$$

$$a_c = \left[ \frac{K_{Ic}}{S \cdot Y \cdot \sigma_{max} \cdot \sqrt{\pi}} \right]^2, \quad (20)$$

$$a_F = \left[ \frac{1}{a_o^{(2-n)/2} + \frac{(2-n)}{2} C \cdot Y^n \cdot \hat{\sigma}_{TFP}^n \pi^{n/2} \cdot N} \right]^{2/(n-2)}. \quad (21)$$

### III. Remarks on material data for fatigue crack growth

The experimental situation can be summarized as follows:

- Fatigue crack rates of austenitics measured at 4 K show large differences (factor 20 - 50); see Fig. 55 of Ref. 5. (If a special austenitic steel is selected for a NET TF or PF coil design, the data  $K_{IC}$ ,  $K_{th}$ ,  $n$ ,  $C$ ,  $E_R$  have to be adapted.)
- The data base for stabilizer copper and aluminium is small as far as the crack growth behaviour at low temperatures is concerned. On the other hand, a good data base is present as far as fatigue strength properties (at ambient temperatures) of commercially available copper and copper-based alloys exist; see Table 10 of Ref. 5 (fatigue strength of OFHC copper at 100 MPa and  $3 \times 10^6$  cycles). At cryogenic temperatures, however, the fatigue strength increases with OFHC copper so that one is on the safe side when using the room temperature data.
- The specific resistivity of the stabilizer material increases with the cycle number; this increase is accompanied by loss of stability. As recent experiments on aluminium show /15/, the residual resistivity reaches saturation after about 1000 cycles, and on saturation high-purity aluminium becomes "fully hard" and behaves elastically as if it were a strong aluminium alloy. The resistivity increase depends on the strain  $\epsilon$ ; for  $\epsilon = 0.3 \%$  the resistivity increases by a factor of about 10 (from 2.4 to 22.3 n $\Omega$  cm). At present there are not enough experimental data to make quantitative allowance for the resistivity increase in the design calculation.
- The data base for thermal and electrical insulation materials under the operational conditions of fusion coils is very small.

- There are only few results for welds with relevant materials; the values of the fracture toughness  $K_{IC}$  of the welds are in general smaller /8, 12, 13, 16/ than  $K_{IC}$  for the parent material. It seems, however, possible to improve them with special filler materials, as shown in Fig. 6 /16/.
- The data basis for the superconductors NbTi and  $Nb_3Sn$  is modest. For NbTi alloys the influence of cycles seems to be small /18, 19/. NbTi alloys are ductile materials. The important effect of fatigue in NbTi composites with copper as stabilizer is mechanical and electrical damage to the copper. Copper has a very low yield stress (in contrast to NbTi) and is plastically deformed at low stress levels. The situation with  $Nb_3Sn$  /19, 20/ is more complex than with NbTi;  $Nb_3Sn$  is a brittle material for which the degradation of the critical current with strain depends highly on the specimens /19/.  
  
For both composite conductors (complex systems with twisted and transposed fine NbTi and  $Nb_3Sn$  filaments embedded in the stabilizer) the influence of fatigue and stress effects on the behaviour of the conductors needs further investigation (shakedown effect /20/ etc.).
- No fatigue crack growth data exist for any of the coil components with respect to liquid helium temperature and radiation (n,  $\gamma$ ) environments. One can imagine that the fracture toughness considerably decreased at low temperatures, where Frenkel pairs form defect clusters. Irradiation in combination with cyclic stresses may also induce phase transitions which may have an adverse influence on the crack growth rate and fracture toughness.



Fig. 6:

Strength-toughness data for fully austenitic welds at 4 K, including comparison with AISI 304 metals at 4 K /16/.

- Stainless steel compositions
- Fe-14 Mn-8 Ni-1 Mo-0.7  
filler material

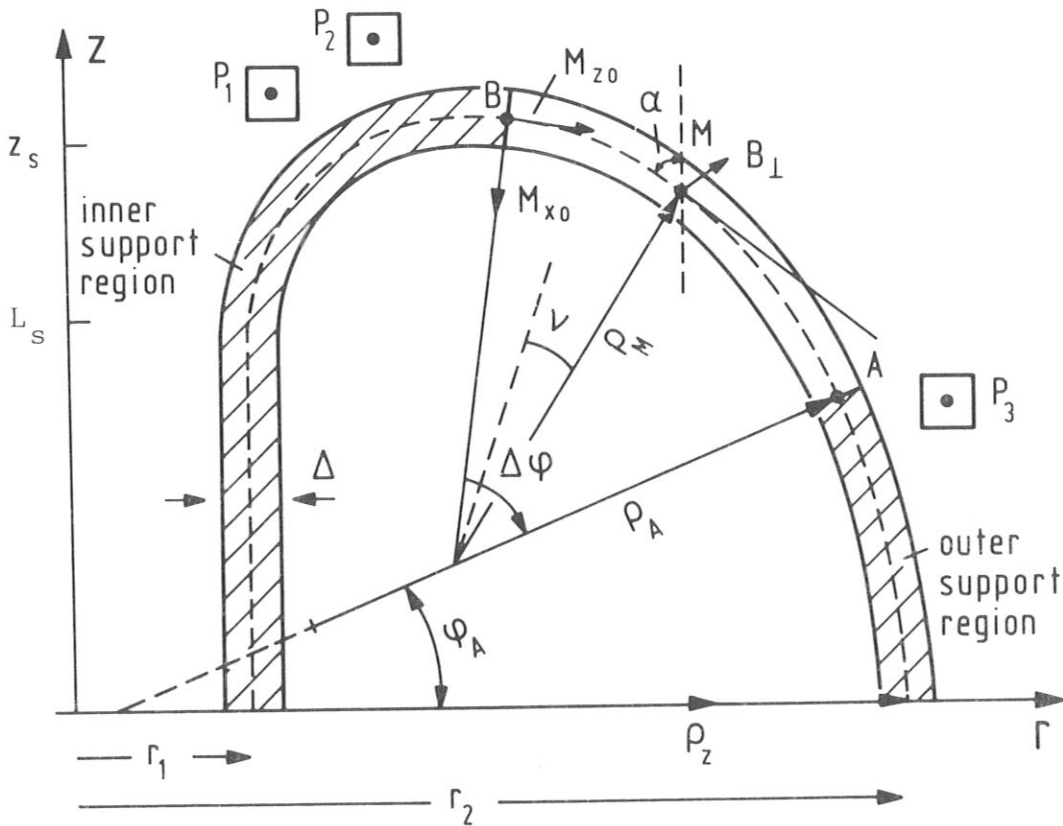
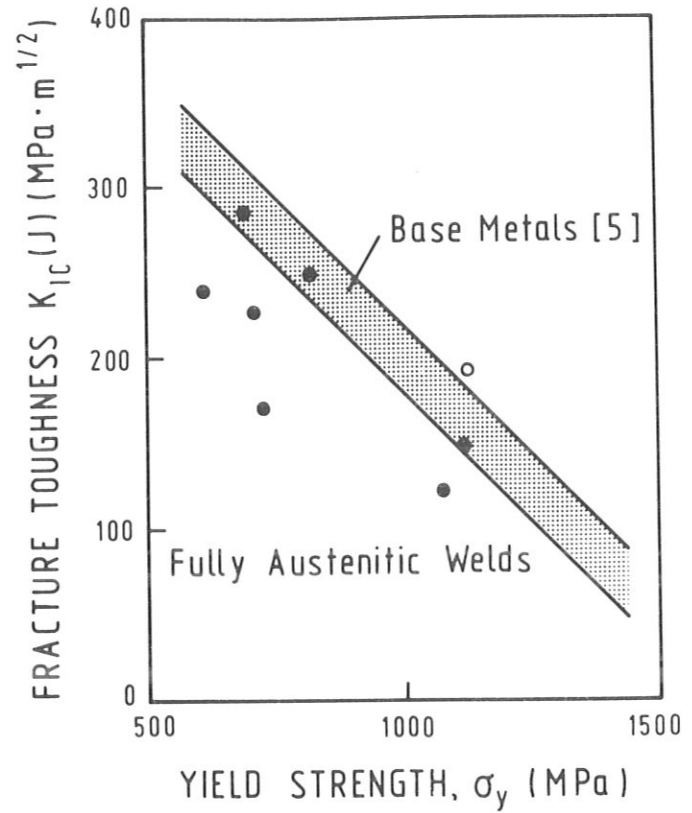


Fig. 7:  $P_F$  coil configuration and support model for the TF coils

#### IV. Analytical Model for the bending and torsional moment calculations

This section describes the analytical model for calculating the bending and twisting moments  $M_x$  and  $M_z$  acting on the unsupported part of the TF coil. The bending stress  $\sigma_{TFP}$  and the shear stress  $\tau_{TFP}$  follow from these moments. Both moments are produced by the Lorentz ( $f = I \cdot B_{\perp}$ ) force per unit length.  $B_{\perp}$  is the magnetic induction produced by the poloidal field coils in the centre M of the unsupported coil region, and I is the total current of one TF coil (see Fig. 7).

As shown in Fig. 7, the poloidal field coil system is modelled by three coils  $P_1$ ,  $P_2$  and  $P_3$ . Double-null and single-null configurations can be properly described by such a coil configuration. The influence of the plasma current is neglected in this section. It is discussed in Appendix II.

The coordinates of  $P_1$ ,  $P_2$  and  $P_3$  are given in the model in the form

$$P_1 = \left\{ \begin{matrix} r_1 + m_1 \Delta \\ z_s + n_1 \Delta \end{matrix} \right\}, \quad P_2 = \left\{ \begin{matrix} r_1 + m_2 \Delta \\ z_s + n_2 \Delta \end{matrix} \right\}, \quad P_3 = \left\{ \begin{matrix} r_2 + m_3 \Delta \\ L_s + n_3 \Delta \end{matrix} \right\},$$

where  $m_1$ ,  $m_2$ ,  $m_3$ ,  $n_1$ ,  $n_2$ ,  $n_3$  are input parameters and  $\Delta$  is the TF coil winding height.

The maximum height of the TF coil centre line  $z_s$  and the height of the straight coil section  $L_s$  are calculated in a preceding part of SUPERCOIL according to Ref. /2/.

The poloidal field coil currents  $I_1$ ,  $I_2$  and  $I_3$  are related to the plasma current  $I$  according to

$$I_1 = l_1 I_p, \quad I_2 = l_2 I_p, \quad I_3 = l_3 I_p.$$

As point design studies show (see, for instance, Ref. /21-23/ a good approximation of the coil currents at the end of the burn phase can be achieved with  $l_1 = 1$ ,  $l_2 = 0$ ,  $l_3 = -1/2$ . Using the currents at the end of the burn phase is justified by numerical calculations /22/ which show that the largest  $f$  values are obtained at this time.

The radii of curvature  $\rho_A$ ,  $\rho_M$  are calculated according to the ideal D-coil concept in /2, 3/, where  $\rho(r)$  is related to  $r$  and to the inboard and outboard centre line coil radii  $r_1, r_2$  by

$$\begin{aligned} \rho &= \frac{1}{2} r \ln (r_2/r_1). \\ &= r \cdot k \end{aligned} \tag{22}$$

It is further assumed that the TF coil is supported against the lateral forces  $f$  by two systems. One is located at the inner part and one at the outer part of the coil. The reason for extending the inner support part in the region where  $\alpha \leq 90^\circ$  (see Fig. 7) is to avoid large stresses due to the large  $f$  values, which also vary very strongly in the region  $\alpha \approx 90^\circ$ .

The coordinates of the points {A} and {M} are calculated with the equations describing the centre line of an ideal D-coil /2/:

$$dr = -\rho(r) \sin \alpha \, d\alpha, \tag{23}$$

$$dz = \rho(r) \cos \alpha \, d\alpha. \tag{24}$$

The radius of curvature is given by eq. (22). The differential equation (23) can be integrated explicitly to give /2/

$$r = r_2 e^{-k} e^k \cos \alpha. \quad (25)$$

For the z-coordinate the integration cannot be done explicitly. To calculate z, an approximate discretization of the coil is used, and  $z(\alpha)$  is calculated by iteration of

$$\Delta z^{n+1} = \rho^n \cos \Delta \alpha \Delta \alpha^{n+1}, \quad (26)$$

where (n+1) is the number of the (n+1) segment and n is the number of the preceding one. The z-coordinate of point {A} is calculated with  $\rho_2$  and  $\alpha = 0$ , and the z-coordinate of {M} with  $\rho_A$  and  $\alpha = \varphi_A$  (see Fig. 7). The coordinates are given by

$$\{A\} = \begin{Bmatrix} r_A \\ z_A \end{Bmatrix} = \begin{Bmatrix} r_2 e^{-k} e^k \cos \varphi_A \\ \rho_2 \sin \varphi_A \end{Bmatrix} \quad (27)$$

$$\{M\} = \begin{Bmatrix} r_M \\ z_M \end{Bmatrix} = \begin{Bmatrix} r_2 e^{-k} e^k \cos(\varphi_A + \Delta \varphi / 2) \\ (\rho_2 - \rho_A) \sin \varphi_A + \rho_A \sin(\varphi_A + \Delta \varphi / 2) \end{Bmatrix}, \quad (28)$$

where  $\rho_2 = r_2 \cdot k$  and  $\rho_A = r_A \cdot k$ .

$\varphi_A$  and  $\Delta \varphi$  define the supported regions and are treated as given quantities in this section.

The distances between M and the centre of the poloidal field coils are

$$r_1 = \overline{P_1 M} = [(r_1 + m_1 \Delta - r_M)^2 + (z_s + n_1 \Delta - z_M)^2]^{1/2}, \quad (29)$$

$$r_2 = \overline{P_2 M} = [(r_1 + m_2 \Delta - r_M)^2 + (z_s + n_2 \Delta - z_M)^2]^{1/2}, \quad (30)$$

$$r_3 = \overline{P_3 M} = [(r_2 + m_3 \Delta - r_M)^2 + (L_s + n_3 \Delta - z_M)^2]^{1/2}. \quad (31)$$

The magnetic induction  $B_{\perp}$  at M follows from

$$B_{\perp} = B_r \cdot \cos \alpha + B_z \sin \alpha, \quad (32)$$

where the magnetic induction values are given by /30/

$$B_r = \frac{I_0}{2\pi} \left[ \frac{\ell_1 I_p}{r_1^2} (z_M - z_{p1}) + \frac{\ell_2 I_p}{r_2^2} (z_M - z_{p2}) + \frac{\ell_3 I_p}{r_3^2} (z_M - z_{p3}) \right], \quad (33)$$

$$B_z = - \frac{I_0}{2\pi} \left[ \frac{\ell_1 I_p}{r_1^2} (r_M - r_{p1}) + \frac{\ell_2 I_p}{r_2^2} (r_M - r_{p2}) + \frac{\ell_3 I_p}{r_3^2} (r_M - r_{p3}) \right]. \quad (34)$$

The magnetic force per unit length follows from  $I \cdot B_{\perp}$ . The bending moment  $M_x$  and twist moment  $M_z$  (the calculation is described in Appendix I) produce tensile stresses  $\sigma_{TFP}$  and shear stresses  $\tau_{TFP}$ . The stresses are given by

$$\sigma_{TFP} = \frac{M_x \cdot B'}{2 I_x} \quad (35)$$

and

$$\tau_{TFP} = \begin{cases} \frac{M_z (3+1.8 \Delta'/B')}{B' \Delta'^2} & B' \geq \Delta' \\ \frac{M_z (3+1.8 B'/\Delta')}{\Delta' B'^2} & B' \leq \Delta' \end{cases} \quad (36)$$

where  $I_x$  is the moment of inertia

$$I_x = \Delta' \cdot B'^3 / 12, \quad (37)$$

$B'$  is the axial width and  $\Delta'$  is the radial width, both of them including the coil casing ( $B' = B + \delta_c$ ,  $\Delta' = \Delta + \delta_c$ ).

The calculation of the shear stress  $\tau_{TFP}$  takes into account the wrapping effect /14/.

The torsional rigidity  $C$  of the coil (with rectangular cross-sectional area) is calculated from eqs. (38,39) /14, 29/:

$$C = \begin{cases} B' \Delta'^3 [1/3 - 0.21 \Delta'/B' (1 - 1/12 (\Delta'/B')^4)] \cdot G & B' \geq \Delta' \\ \Delta' B'^3 [1/3 - 0.21 B'/\Delta' (1 - 1/12 (B'/\Delta')^4)] \cdot G & B' \leq \Delta' \end{cases} \quad (38)$$

$$G = E / (1 + \nu). \quad (39)$$

$G$  is the shear modulus; see App. I. The maximum tensile stresses  $\sigma_{TFP,max}$  and  $\tau_{TFP,max}$  follow from eqs. (35) and (36) with the maximum moments  $M_x$  and  $M_z$ . The moments change along the arc, as shown in Fig. 8, where  $M_x$  and  $M_z$  are plotted versus the angle  $\rho$  (see Figs. 8 and A1; in Fig. 8 the special case for semi-circle is shown). The procedure to find the maximum of  $M_x$  and  $M_z$  for arbitrary  $\Delta\rho$  is described in Appendix I.

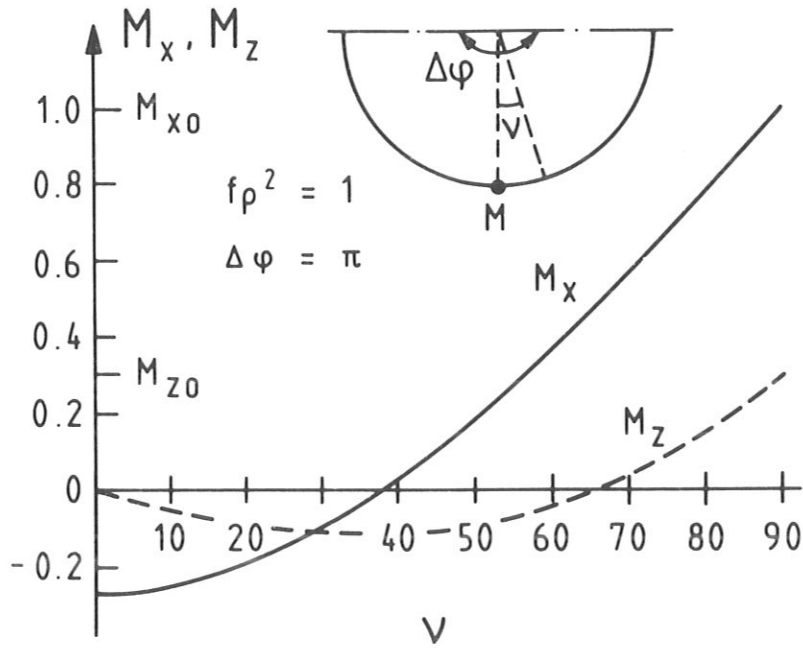


Fig. 8: Variation of  $M_x$  and  $M_z$  versus  $\rho$  for  $\Delta\rho = \pi$ . For symmetry reasons the moments are only shown for half of the semi-circle (see insert in Fig. A1).

#### V. Numerical calculations

The analytical model for calculating the mechanical stresses (as described in Sect. IV and in Appendix I) is tested by means of numerical calculations.

The mechanical stresses are calculated with the STELLA computer program system /24/. The main components of STELLA are the EFFI /25/ and SAP /26/ computer programs. The EFFI program allows the magnetic fields, forces and inductances to be calculated for general three-dimensional current distributions. The magnetic volume forces calculated with EFFI are needed

as input for the SAP finite-element program, with which the mechanical stresses and deformations are calculated.

The numerical calculation procedure starts by determining the D-shape of the toroidal field coils. The theoretical basis for the computer program with which the contour of the D-coil is calculated is described in Ref. /3/. The main input data are taken from Ref. /22/, where the parameter set for NET 22 B is presented. The main input data are:  $r_1 = 2.125$  m,  $r_2 = 8.85$  m and  $\Delta = 0.7$  m ( $r_1$  and  $r_2$  are the inboard and outboard centre line coil radii, and  $\Delta$  is the radial winding thickness, see Fig. 7).

The "general current element" (GCE) is used for the magnetic force calculation with EFFI. The GCE subdivision for the calculation is shown in Fig. 9. The subdivision into GCE was carried out with the MGCE program /24/.

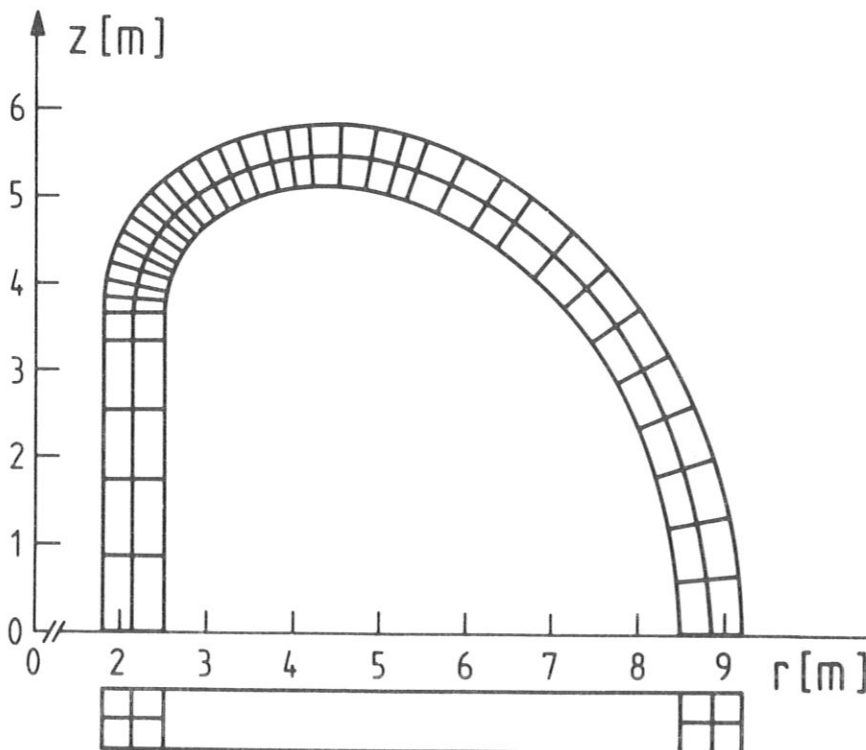


Fig. 9:

Subdivision of the D coil into GCEs. The same subdivision is used for the finite-element calculations with SAP.



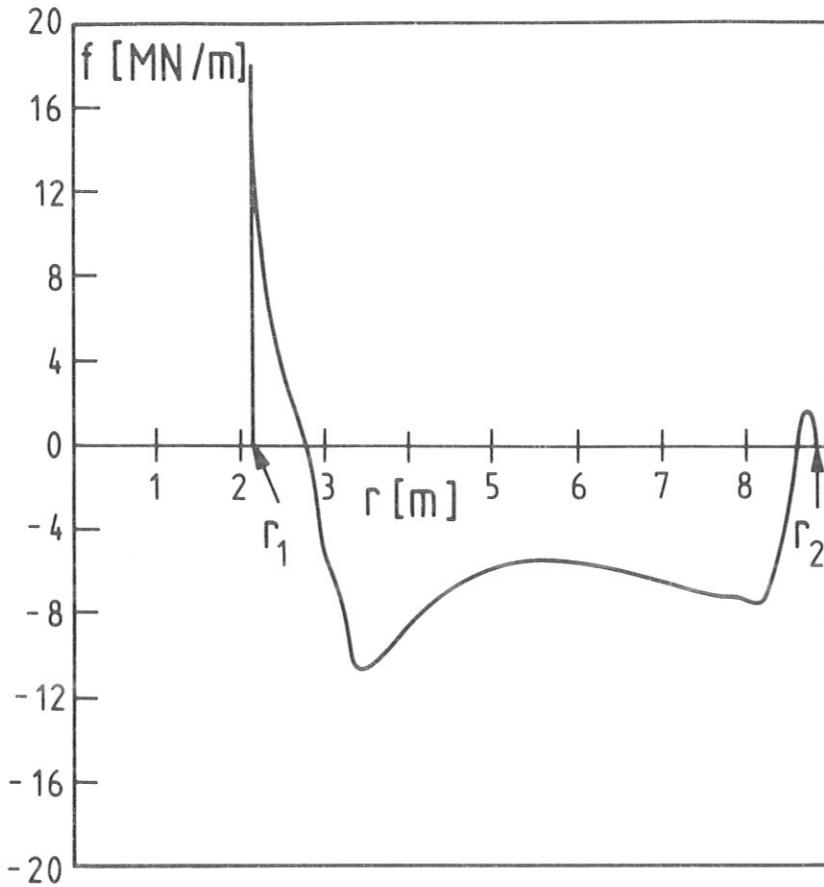


Fig. 10:  
Lateral forces per unit length for the upper part of the D-coil shown in Fig 9. Forces are calculated with the EFFI computer program.

The data for the PF coils are listed in Table 3 /22/. The currents in the PF coils correspond to the time at the end of the burn phase.

Coil number	$r_o$ [m]	$z_o$ [m]	$\Delta r$ [m]	$\Delta z$ [m]	I [MA]
1	9.65	2.5	0.35	0.7	-6.1
2	4.05	6.75	0.5	0.5	-2.2
3	2.275	6.125	0.75	0.75	11.1
4	1.55	4.75	0.4	0.7	5
5	1.55	1.25	0.4	2.5	-25

Table 3: Position and currents of the PF coils.  $r_o$  and  $z_o$  are the coordinates of the coil centre, and  $\Delta r$  and  $\Delta z$  the radial and axial widths, respectively.

Figure 9 shows only the coils (or coil part) above the r-y plane; the force calculations also includes the coils below the r-y plane.

The lateral force per unit length  $f$  for the upper D-coil part is shown in Fig. 10.  $f$  is the force (per unit length) acting on the centre line.

The input data for the SAP computer program was prepared with the FENGGEN and SHAP computer programs [24, 27]. The FENGGEN computer program calculates the coordinates of the nodal points from the coordinates describing the GCEs. The calculation of the nodal forces from the volume force is carried out with the SHAP computer program. For the stress calculations the 20-node isoparametric element [27] is used.

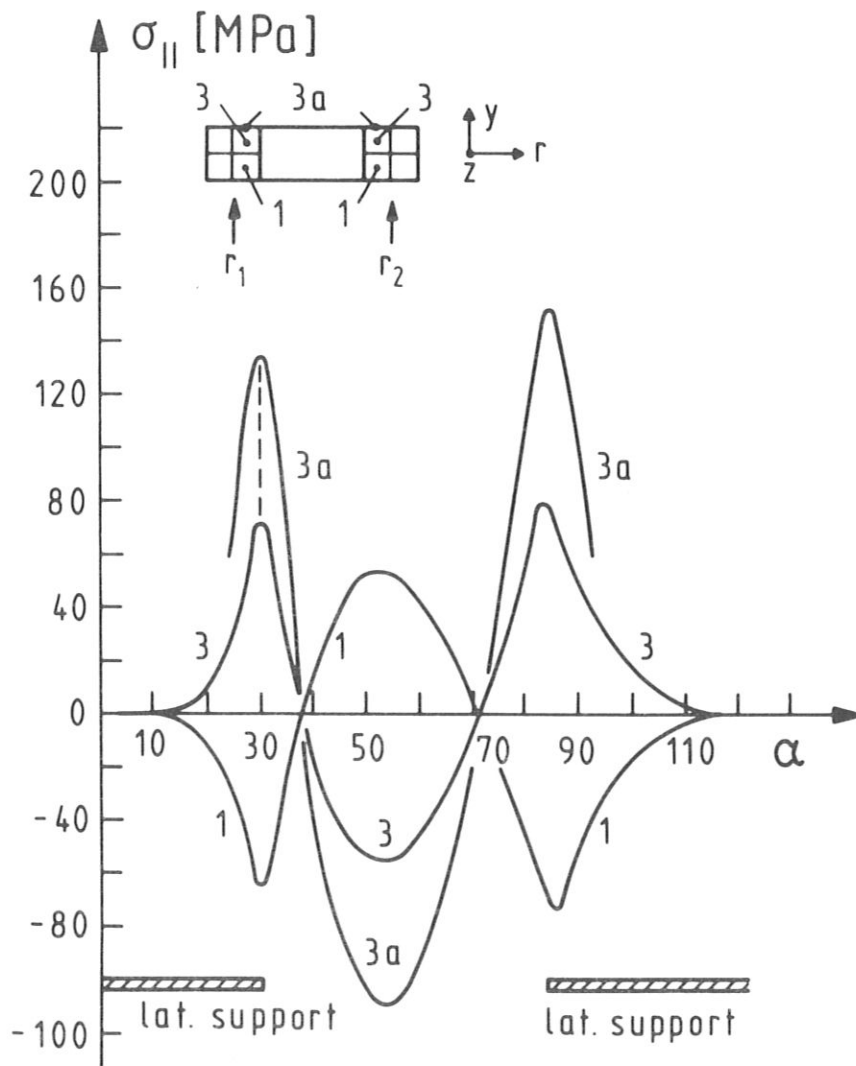


Fig. 11

Tangential stress  $\sigma_{II}$  versus the angle  $\alpha$  ( $\alpha$  is the angle between the tangent on the centre line and the vertical axis, see Fig. 7). The stress output locations are 1, 3 and 3a (see insert).

In order to get only the  $f$  forces produced by the poloidal field coils, the volume forces in the TF coil were calculated with and without the poloidal field coils and finally the difference was taken. The finite-element calculations were carried out with a lateral support in the regions (only half a coil is considered for symmetry reasons)  $0 \leq \alpha \leq 30$  and  $84 \leq \alpha \leq 180$  and in the straight part of the D-coil. In an iterative process (several finite-element runs) the boundary conditions were optimized until the lateral nodal points in the support regions were only under pressure.

Results are shown in Figs. 11 and 12. Figure 11 shows the tensile (tangential) stress  $\sigma_{\parallel}$  for three stress output locations. The locations 1 and 3 are the centres of the two inner elements; the centres are located at  $y = -0.175$  and  $0.175$  cm (the width of the coil winding is  $0.7$  m). The location 3a is at the lateral surface of the winding package at  $y = 0.35$  m. The coil winding can glide within the support area in the  $r$  and  $z$  directions (the displacements  $\Delta r, \Delta z$  of the nodal points in the support region are free  $\Delta r, \Delta z \neq 0$ ). The stress state therefore extends into the supported region of the coils with  $\alpha < 30^\circ$  and  $\alpha > 84^\circ$ ). As can be seen, the maximum stresses are at the transition regions where the support begin or ends. The stress state of location 1 is "negative" with respect to the stress state of location 3; if location 3 is under tension ( $\sigma_{\parallel} > 0$ ), the stress state of location 1 is under compression ( $\sigma_{\parallel} < 0$ ). The maximum stress at the lateral side is  $152$  MPa. This stress pattern is in agreement with the beam bending theory when a beam is loaded with forces in the  $y$ -direction.

The analytical model for the stress calculation is based on the assumption that the arc is kept fixed in the support region; when this boundary condition is translated into finite-element language,  $\Delta r$  and  $\Delta z$  also have to be kept fixed ( $\Delta r, \Delta z = 0$ ) in the support region. The tangential stress  $\sigma_{||}$  with such boundary conditions is shown in Fig. 12.

The main differences between Fig. 11 ( $\Delta r, \Delta z \neq 0$  in support) and Fig. 12 ( $\Delta r, \Delta z = 0$ ) are: larger maximum stressed at the transition from the supported and unsupported regions in Fig. 12 and smaller pressure values at the centre of the arc (at  $\varphi = \varphi_a + \Delta \varphi/2$ ).

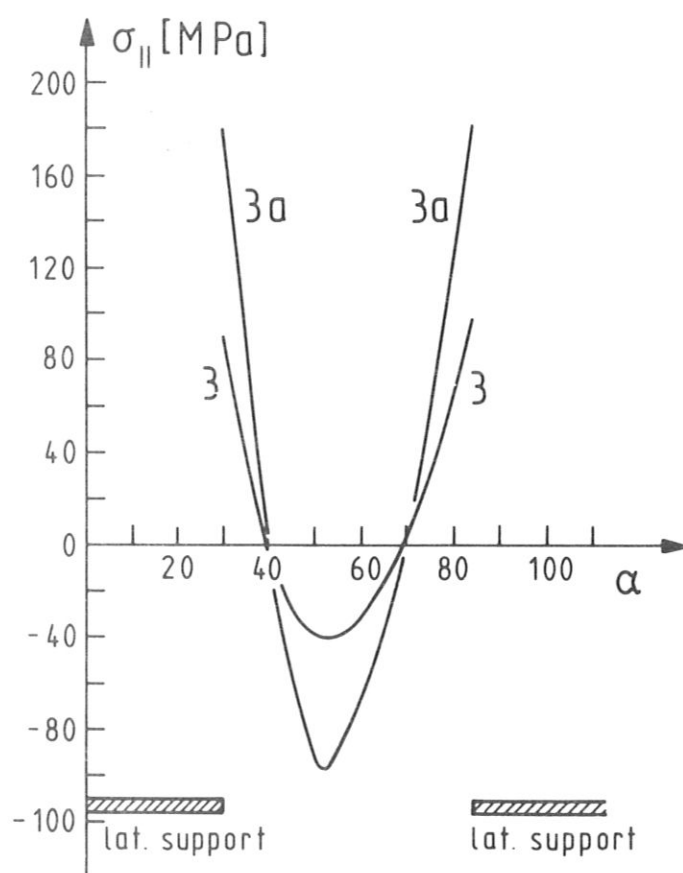


Fig. 12: Tangential stress versus  $\alpha$  at the stress output locations 3 and 3a (see Fig. 11). The boundary conditions are changed with respect to Fig. 11.

## VI. Comparison between numerical and analytical results

The analytical model described in Sect. IV is compared with numerical results to check the accuracy of the magnetic force and mechanical stress calculations.

The lateral forces per unit length exerted on the centre line of the D-coil (upper part) by the poloidal field coils (see Table 1) are shown in Fig.13.

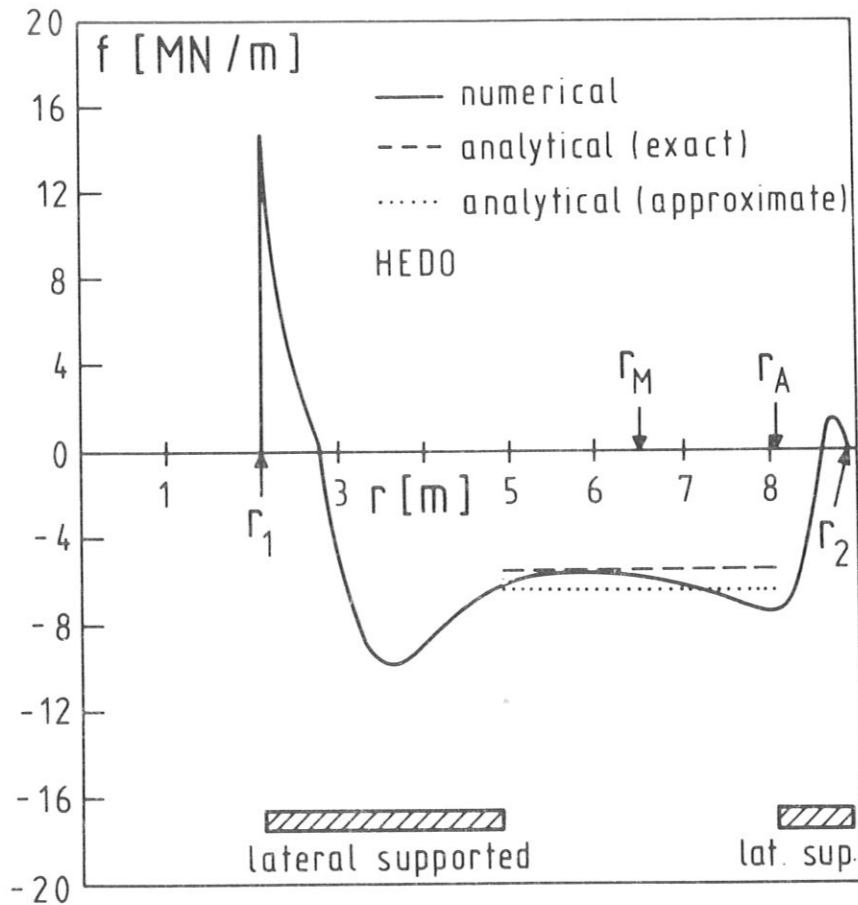


Fig. 13: Comparison between numerically and analytically calculated magnetic forces.

The numerical magnetic forces are calculated with the HEDO program /7/. Figure 10 shows the magnetic forces calculated with the EFFI computer program; the agreement between the curves in Figs. 10 and 13 is good, with the exception of the location where the curved part of the D enters the straight section. The analytical values in the unsupported region are shown.

Two analytical values are shown in Fig. 13, one exact and one approximate. The exact value is calculated with the exact position and currents described in Table 1. The approximate value is calculated on the simplifying assumption that (see Fig. 7)

$$I_1 = I_P (10.77 \text{ MA}), \quad m_1 = 0, \quad n_1 = 1,$$

$$I_2 = 0,$$

$$I_3 = -\frac{1}{2} I_P, \quad m_3 = 1, \quad n_3 = 1.$$

The results of Fig. 13 refer to the double-null configuration NET 22 B. The model described in Sect. IV is also applicable to a single-null divertor configuration as shown in Fig. 14. In Fig. 14 numerical values taken from Ref. /23/ are compared with analytical results in the region where the coil is not laterally supported. The  $f$  values for the single-null configuration are higher than for an equivalent double-null configuration (equivalent means that the TF coil configurations are identical, except for the fact that only the poloidal field coils differ). The analytical calculations are based on the three-coil model with the currents -8.25, 17.68 and -8.56 MA. The currents are higher than those for a double-null configuration.

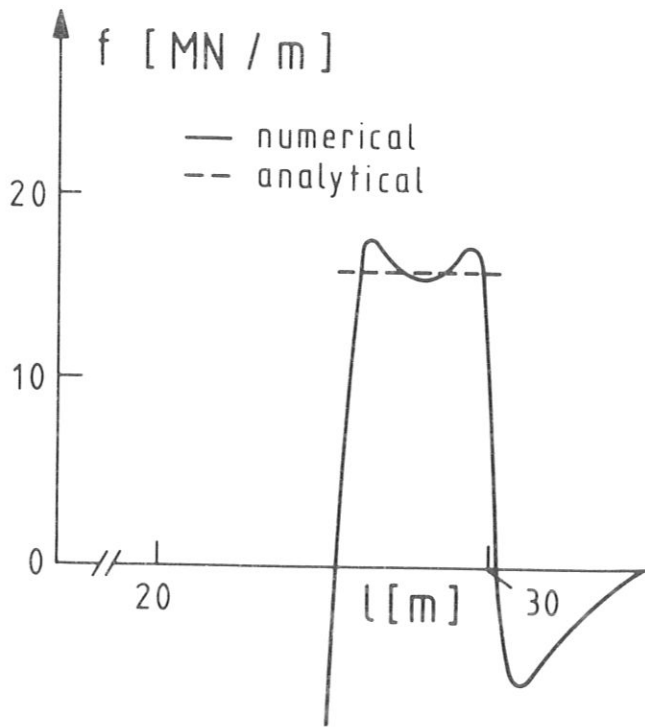


Fig. 14:

Lateral forces per unit length  
for the single null  
configuration NET 3 A /23/.

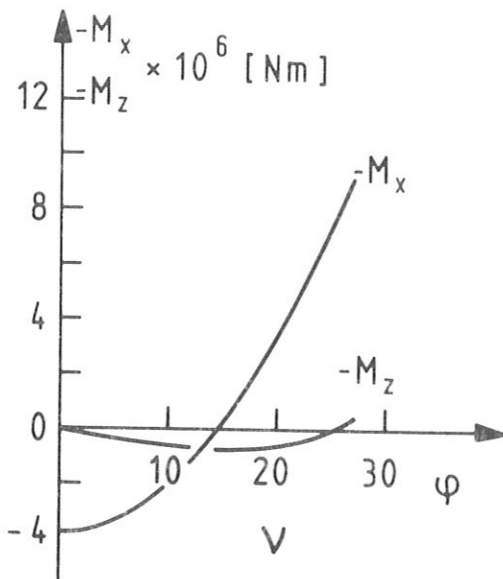


Fig. 15:

Bending and torsional moments  
acting on an arc with lateral  
forces.

The analytical stress calculations for the NET 22B configurations are made with the following data:

$$\Delta = B = 0.7 \text{ m (radial and axial widths of the winding),}$$

$$\rho_a = 30^\circ,$$

$$\Delta \rho = 54^\circ,$$

$$\rho_M = 4.56 \text{ m (calculated with eq.25 ).}$$

The bending and twist moments  $M_x$  and  $M_z$  acting on half of a beam in the unsupported region are shown in Fig. 15 (see Appendix I). The stresses  $\sigma_{11} = \sigma_{TFP}$  and  $\tau = \tau_{TFP}$  are obtained from the moments with eqs. (35), (36).

The tangential stress  $\sigma_{||}$  calculated numerically and analytically is compared in Fig. 16. The stress output location is 3a (lateral boundary at  $y = 0.35$  m; see Fig. 11). The numerical curve is taken from Fig. 12.

The difference in the maximum stress at the location where the support structure at  $\alpha = 84^\circ$  begins is 20 MPa (11 %). The difference in the location of the minimum is mainly due to the fact that the analytical curve is calculated with an average radius of curvature  $\rho = \rho_M$ , whereas in the

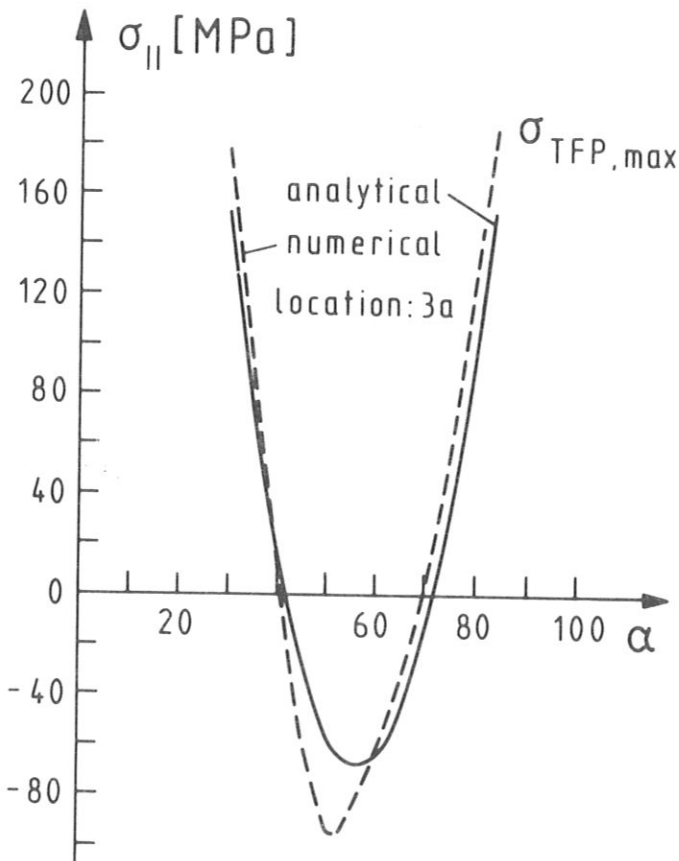


Fig. 16:

Comparison of the tangential stress  $\sigma_{||}$  calculated with analytical and numerical methods for the unsupported part of a NET 22B TF coil. The stress output location is 3<sub>a</sub> (see Fig. 13).



numerical calculation the radius of curvature changes from a larger one at  $\alpha \sim 30^\circ$  to a smaller one at  $\alpha \approx 80^\circ$ . The analytically calculated shear stresses are below 10 MPa; a maximum value of 9 MPa was found. The numerically calculated maximal values are in the range of 5 MPa; the values are uncritical.

One method of decreasing the  $\sigma_{\parallel}$  values is to increase the coil dimensions. If the inner coil casing is taken into account (the axial width increases from 0.7 m to 1 m and the radial width from 0.7 to 0.8 m), the maximum  $\sigma_{\parallel} = \Delta\sigma_{TFP}$  decreases from 161 MPa to 70 MPa.

# Appendix I

## Calculation of the bending and torsional moments for an arc with perpendicular force loading

The part of the D-coil not laterally supported (see Fig. 7) can be approximated by an arc. The corresponding radius is given by  $\rho_M = r_M \cdot k$  ( $r_M$  is given by using eq. (25)). The mechanical loading of the arc follows from the line force  $f$ , which acts perpendicularly to the arc axis. Figure A1 shows a schematic view of the arc with the definitions of angles, moments and forces.

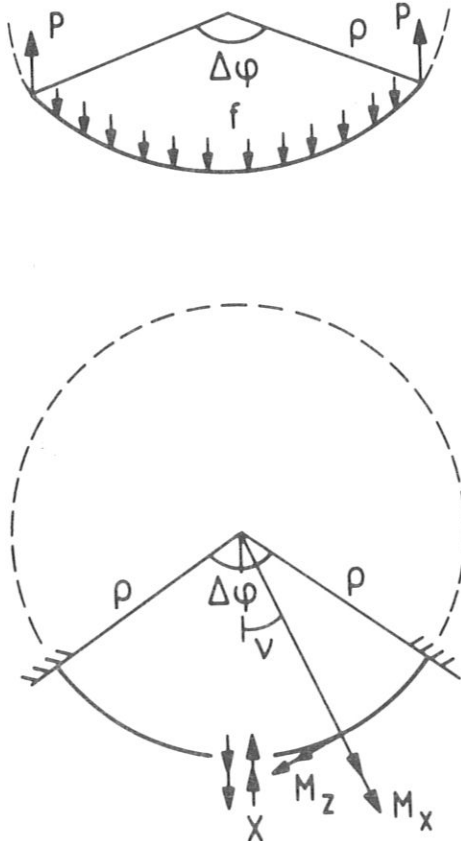


Fig. A1:

Schematic view of the arc loaded with a constant line force  $f$ .

The reaction force  $P$  and the reaction moment  $M_{x0}$  ( $\psi = \Delta \varphi / 2$ ) are given by

$$P = f \rho \Delta \varphi / 2 \quad (A1)$$

$$M_{x0} = \rho^2 f (1 - \cos \Delta \varphi / 2) - X \cos \Delta \varphi / 2, \quad (A2)$$

respectively.  $X$  cannot be calculated for equilibrium conditions because the problem is statically undetermined. To calculate  $X$  (and  $M_x, M_z$ ), the principle of virtual work is used:

$$\frac{\partial U}{\partial X} = 2 \frac{\partial}{\partial X} \int_0^{\Delta \varphi / 2} \left( \frac{M_x^2}{2EI_x} + \frac{M_z^2}{2C} \right) \rho dv \equiv 0 \quad (A3)$$

$M_x$  and  $M_z$  are the moment with respect to the x- and z-axes.  $I_x$  is the moment of inertia about the local x-axis and  $C$  is the torsional rigidity, related to  $I_p$  as  $C = G \cdot I_p$  ( $G$  = modulus of rigidity; see rels. 38, 39)

$M_x$  and  $M_z$  are given by

$$M_x = f \rho^2 (1 - \cos v) - X \cos v, \quad (A5)$$

$$M_z = f \rho^2 (v - \sin v) - X \sin v, \quad (A6)$$

With

$$\frac{\partial M_x}{\partial X} = -\cos v, \quad \frac{\partial M_z}{\partial X} = -\sin v \quad (A7)$$

eq. (A3) yields

$$\begin{aligned} \frac{1}{EI_x} \{ f \rho^2 [\sin(\Delta\varphi/2) - \frac{1}{4} \sin \Delta\varphi - \frac{1}{4} \Delta\varphi] - \frac{X}{4} [\Delta\varphi + \sin \Delta\varphi] \} + \\ + \frac{1}{C} \{ f \rho^2 [\sin(\Delta\varphi/2) - \frac{\Delta\varphi}{2} \cos(\Delta\varphi/2) - \frac{\Delta\varphi}{4} + \frac{1}{4} \sin \Delta\varphi] - \frac{X}{4} [\Delta\varphi - \sin \Delta\varphi] \} = 0 \end{aligned} \quad (A8)$$

The moment  $X$  can be calculated from eq. (A8); substituting it in eq. (A5) and (A6) yields  $M_x$  and  $M_z$ .

For the case  $\Delta\varphi = \pi$  the moments  $M_x$  and  $M_z$  are

$$M_x = f \rho^2 (1 - \frac{4}{\pi} \cos v), \quad (A9)$$

$$M_z = f \rho^2 (\varphi - \frac{4}{\pi} \sin v). \quad (A10)$$

The torsional moment  $M_{z0}$  ( $\nu = 90^\circ$ ) is then

$$M_{z0} = f \rho^2 \left[ \frac{\pi}{2} - \frac{4}{\pi} \right], \quad (A11)$$

which for this special case shows agreement with Rev. /14/.

In the following, the simplification of eq. (A8) and the procedure for finding the maxima of  $M_x$  and  $M_z$  are described.

With the relations

$$C = G \cdot I_p \quad (A12)$$

$$\text{and} \quad G = \frac{E}{2(1+\nu)}, \quad (A13)$$

where  $G$  is the shear modulus and  $\nu$  is the Poisson ratio (the value of  $\nu$  is set equal 0.3), the moment  $X$  is given by

$$X = 4 f g^2 \frac{I_p / I_x [\sin(\Delta\psi/2) - \Delta\psi/4 - (\sin \Delta\psi)/4] + 2.6 [\sin(\Delta\psi/2) - (\Delta\psi \cos(\Delta\psi/2))/2 - \Delta\psi/4 + (\sin \Delta\psi)/4]}{I_p / I_x [\Delta\psi + \sin \Delta\psi] + 2.6 [\Delta\psi - \sin \Delta\psi]}, \quad (A14)$$

$I_p$  and  $I_x$  being defined by eqs. (38) and (A12).

To find the maximum values of  $|M_x|$  and  $|M_z|$ , two values have to be compared for each moment.

For  $|M_x|$  it is the values at  $\nu = 0$  and at  $\nu = \Delta\psi/2$  (see Fig. 8) that have to be compared. At  $\nu = 0$  the moment  $M_x$  is  $-X$ ; with increasing  $\nu$ ,  $M_x$  also increases. The maximum moment  $|M_{x,\max}|$  yielding the maximum

$\theta_{TFP}$  ( $\theta_{TFP,max}$ ) is given by

$$|M_{x,max}| = \max \{ |X|, |M_x|_{\nu = \Delta\varphi/2} \}. \quad (A15)$$

The maximum  $|M_z|$  value follows from a comparison of  $M_z$  at

$$\nu_m = \cos^{-1} (1/(1+X/f\rho^2)) , \quad (A16)$$

where the minimum (see Fig. 8) is located, and at  $\nu = \Delta\varphi/2$  (for  $\Delta\varphi = \pi$ , as shown in Fig. 8, the angle  $\nu_m$  according to eq. (A16) is  $\sim 38^\circ$ ):

$$|M_{z,max}| = \max \{ |M_z|_{\nu = \nu_m}, |M_z|_{\nu = \Delta\varphi/2} \} \quad (A17)$$

It is evident that in this case  $\Delta\varphi/2$  has to be larger than  $\nu_m$ ; if not,  $|M_{z,max}|$  is given by  $|M_z|_{\nu = \Delta\varphi/2}$ .

## Appendix II

### Influence of the plasma current on the magnitude of the magnetic force in the unsupported region

The calculations in Sect. IV neglect the plasma current  $I_p$ . In the following, the contribution of the plasma current to  $B_\perp$  (or  $f$ ) is discussed. For this reason we compare the  $B_\perp$  values produced by the poloidal field coil 1, which is furthest from the centre M of the



difference is due to the different  $\Delta\alpha$  values and is not so much a consequence of the distances, which differ by only 20 %. The  $f$  value produced by the current element 1 is only about 1/15 of that of element 0.

The conclusion is that the plasma current elements which are located near the top practically do not contribute to the Lorentz force in the support region and "concentrated" currents in the plasma centre have a small influence on  $f$ .

A concentration of the total plasma current  $I_p$  in 0 would be an over-estimate of the influence of the plasma current because the upper element practically do not contribute to  $B_z$ . An adequate approximation would be to concentrate half of the plasma current in 0. The magnetic field formulas

(33) and (34) are then written as

$$B_r = \frac{\mu_0}{2\pi} \left[ \frac{\ell_1 I_p}{r_1} (z_M - z_{P1}) + \frac{\ell_2 I_p}{r_2} (z_M - z_{P2}) + \frac{\ell_3 I_p}{r_3} (z_M - z_{P3}) + \frac{1}{2} \frac{I_p}{r_4} z_M \right] \quad (33')$$

$$B_z = - \frac{\mu_0}{2\pi} \left[ \frac{\ell_1 I_p}{r_1} (r_M - r_{P1}) + \frac{\ell_2 I_p}{r_2} (r_M - r_{P2}) + \frac{\ell_3 I_p}{r_3} (r_M - r_{P3}) + \frac{1}{2} \frac{I_p}{r_4} (r_M - r_0) \right] \quad (34')$$

$$r_4 = [(r_M - r_0)^2 + z_M^2]^{1/2} \quad (A19)$$

The relative error in the magnetic force calculations of this report is in the range of 16 % when the plasma current is neglected.

The stress values with plasma current are smaller than those calculated without plasma current for cases where the point M (see Fig. 7) is located between the PF coils 1 and 3.

### Appendix III

#### List of input parameters

Table A 1 lists the input parameters for the TF lifetime calculation. The values of the parameters with a cross as symbol (+) are calculated in preceding parts of the SUPERCOIL computer program.

#### Acknowledgements

The author wishes to express his thanks to K. Borrass for clarifying and stimulating discussions. Thanks are also due to H. Gorenflo for his help with the numerical calculations, S.B. Mukherjee for his reference to the calculation of the bending and torsional moments by using the principle of virtual work and N. Mitchell for discussions on the poloidal coil system of NET design systems.



INPUT

R1 <sup>+</sup>	=	0.21300E+01	(INBOARD CENTRE LINE COIL RADIUS)
R2 <sup>+</sup>	=	0.88500E+01	(OUTBOARD CENTRE LINE COIL RADIUS)
R0 <sup>+</sup>	=	0.58100E+01	(PLASMA RADIUS)
LS <sup>+</sup>	=	0.35000E+01	(STRAIGHT PART OF D)
ZS <sup>+</sup>	=	0.55000E+01	(MAX. HEIGHT OF CENTRE LINE)
DEL <sup>+</sup>	=	0.70000E+00	(RADIAL WIDTH OF TF COIL WINDING)
B <sup>+</sup>	=	0.70000E+00	(AXIAL WIDTH OF TF COIL WINDING)
DB <sup>+</sup>	=	0.10000E+00	(THICKNESS OF THE COIL CASING)
IP <sup>+</sup>	=	0.11700E+02	(PLASMA CURRENT IN MA)
PL1	=	0.94800E+00	(IDENTICAL TO LI)
PL2	=	0.18800E+00	(IDENTICAL TO L2)
PL3	=	0.57000E+00	(IDENTICAL TO/L3)
PM1	=	0.20000E+00	(IDENTICAL TO M1)
PM2	=	0.33286E+01	(IDENTICAL TO M2)
PM3	=	0.11428E+01	(IDENTICAL TO M3)
PN1	=	0.89280E+00	(IDENTICAL TO N1)
PN2	=	0.17857E+01	(IDENTICAL TO N2)
PN3	=	0.14286E+01	(IDENTICAL TO N3)
AO	=	0.20000E-02	(INITIAL CRACK SIZE)
KIG	=	0.10000E+03	(FRACTURE TOUGHNESS IN MPA)
ALF	=	0.31000E+00	(EXP. for THRESH. STRESS INTEN: R=0)
PN	=	0.37800E+01	(EXPONENT IN PARIS EQ.)
C	=	0.20400E+01	(COEFFICIENT IN PARIS EQ.)
SA	=	0.18000E+01	(SAFETY FACTOR)
Y	=	0.12500E+01	(GEOMETRICAL CORRECTION FACTOR)
ESC <sup>+</sup>	=	0.10000E+06	(YOUNG'S MOD. of SUPERC. IN MPA)
EST <sup>+</sup>	=	0.10000E+06	( " " STABILIZER IN MPA)
ER <sup>+</sup>	=	0.20000E+06	( " " REINF. MAT. IN MPA)
ALFA <sup>+</sup>	=	0.20000E+02	(RATIO FST:FSC)
BETA <sup>+</sup>	=	0.20000E+02	(RATIO FR:FSC)
ASIGT <sup>+</sup>	=	0.25000E+03	(AVERAGE STRESS IN TF IN MPA)
PHIA	=	0.30000E+02	(ANGLE: SEE FIG. 7)
DEPHI	=	0.54000E+02	(ANGLE FOR UNSUPP. REGION)
CN <sup>+</sup>	=	0.10000E+01	(NUMBER OF BURN CYCLES IN MEGAC.)
BMAX <sup>+</sup>	=	0.11000E+02	(MAXIMUM MAGNETIC FIELD)
NN <sup>+</sup>	=	16	(NUMBER OF COILS)

Table 1: Input parameters for the lifetime calculations

## REFERENCES

- /1/ K. Borrass, M. Söll: "SUPERCOIL, a Layout Model for Tokamaks with Superconducting TF coils", Max-Planck-Institut für Plasmaphysik, Report IPP 4/207, June 1982
- /2/ J. Raeder: "Some analytical results for toroidal magnetic field coils with elongated minor cross-sections". Max-Planck-Institut für Plasmaphysik, Report IPP 4/141, Sept. 1976
- /3/ M. Söll: "Bending-free Shapes of Toroidal Magnet Systems". Interner Bericht No. 19, Projekt Systemstudien, Max-Planck-Institut für Plasmaphysik, Garching.
- /4/ K.-H. Schwalbe: "Bruchmechanik metallischer Werkstoffe". Carl Hanser Verlag München Wien 1980
- /5/ A. Nyilas: "Fatigue Data Compilation and Evaluation of Fatigue on Design". Kernforschungszentrum Karlsruhe, Primärbericht, Dez. 1984
- /6/ R.W. Hertzberg: "Deformation and fracture mechanics of engineering materials". John Wiley & Sons, New York (1976)
- /7/ P. Martin, H. Preis: "Programmbeschreibung und Benutzeranleitung zum Magnetfeld-Computer-Programm HED02 ". Max-Planck-Institut für Plasmaphysik, Report IPP III/34 (1977)
- /8/ A. Nyilas, H. Krauth, E. Lohse: "Kriterien für den Einsatz von hochbelasteten, dickwandigen, austenitischen Schweißnähten im 4-Kelvin Bereich": DVS-Berichte 75, 1982, p. 200
- /9/ R.L. Tobler, R.P. Reed: "Fatigue crack growth rates of structural alloys at 4K". Adv. in Cry. Eng., Vol. 22, Plenum Press, 1975, p. 35
- /10/ T.A. Whipple, H.I. McHenry, D.T. Read: Welding Journal 60, 1981, 72
- /11/ K. Shiraishi: IEA Workshop on special materials for fusion, Culham Lab. 1982
- /12/ A. Nyilas, H. Krauth: "Use of heavy section austenitic welds for 4K service". Kernforschungszentrum Karlsruhe, Primärbericht 03.02.01P26H. Nov. 1981
- /13/ A. Nyilas, H. Krauth, M. Metzner, D. Munz: "Fatigue response of materials used in large superconducting magnets for fusion technology". Proc. of Fatigue 84, 2nd Intern. Conf. on Fatigues and Fatigue Thresholds, Birmingham 1984, Vol. III, p. 1637

- /14/ S. Timoshenko: "Strength of Materials, Part I Elementary, Theorie and Problems". VNR Company, New York, 1976
- /15/ K.T. Hartwig, G.S. Yuan, P. Lehmann: "The effects of low temperature fatigue on the RRR and strength of pure aluminium". Applied Superconductivity Conference 1984, IEEE Tr. on Magnetism, MAG-21, 1985, 161
- /16/ R.L. Tobler, R.E. Trevisan, R.P. Reed: "Tensile and fracture properties of an Fe-14Mn-8Ni-1Mo-0.7C fully austenitic weld metal at 4K". Cryogenics, Vol. 25, 1984, 447
- /17/ R.G. Forman, V.E. Kaerney, R.M. Engle: "Numerical analysis of crack propagation in cyclic loaded structures". J. Base Eng. Trans. ASME 89 (1967) 459
- /18/ E.S. Fisher, S.H. Kim, A.P.L. Turner: "Cyclic stress effects in transport properties of superconducting composite materials" 6th International Cryogenic Engineering Conference, p. 390
- /19/ J.W. Ekin: "Fatigue and stress effect in NbTi and Nb<sub>3</sub>Sn multifilamentary superconductors". Cryogenic Engineering Conference/International Cryogenic Materials Conference, University of Colorado, Boulder, 1977, Advances in Cryogenic Eng., Vol. 24, 1978, pp. 306-3165
- /20/ St.F.Cogan, R.M. Rose: "Fatigue effects in unidirectional composites: application to Nb<sub>3</sub>Sn superconductors". Appl.Phys.Lett. 35 (11), 1979 (884)
- /21/ E. Coccoresse, R. Martone, N. Mitchell: "NET 3A Parameter Set Definition". Report NET/IN/84-098
- /22/ E. Coccoresse, N. Mitchell: "Parameter Set for NET 22B". Report NET/IN/85-049
- /23/ N. Mitchell: "Global Stress Analysis of the Toroidal Field Coils for NET 3A and NET 22B". Report NET/85/K/100-R-01
- /24/ H. Gorenflo, M. Söll: "STELLA - a computer program system for calculating magnetic fields, forces and mechanical stresses for twisted stellarator coil systems". Interner Bericht 17, Projekt Systemstudien des Max-Planck-Instituts für Plasmaphysik, July 1981
- /25/ S.J. Sackett: "EFFI - a code for calculating the electromagnetic field, force and inductance in coil systems of an arbitrary geometry. User's Manual", Lawrence Livermore Laboratory, Report UCID-17621, 1977

- /26/ "SAPV2 - a structural analysis program for static and dynamic response of linear systems. User's Manual". University of Southern California, Department of Civil Engineerig Los Angeles (1977).
- /27/ M. Söll, O. Jandl, H. Gorenflo: "Mechanical Stress Calculations for Toroidal Field Coils by the Finite Element Method". Max-Planck-Institut für Plasmaphysik, Report IPP 4/142, Sept. 1976
- /28/ H.M. Westergaard: "Bearing Pressures and Cracks". J.Appl.Mech. 6 (1939) 49
- /29/ R.J. Roark, W.C. Young: "Formulas for Stress and Strain", McGraw-Hill, New York, 1975
- /30/ G. Oberdorfer: "Lehrbuch der Elektrotechnik, Band 1", R. Oldenburg, München 1961.